This is a preprint version of the article published in:
Journal of Applied Physics, Vol. 116, No. 3, 034905 (2014).
http://dx.doi.org/10.1063/1.4890218

Please, cite this document as:
T. G. ZIELIŃSKI. "Microstructure-based calculations and experimental results for sound absorbing porous layers of randomly packed rigid spherical beads." *Journal of Applied Physics*, Vol. **116**, No. 3, 034905 (2014).
DOI: 10.1063/1.4890218

Microstructure-based calculations and experimental results for sound absorbing porous layers of randomly packed rigid spherical beads

TOMASZ G. ZIELIŃSKI
Institute of Fundamental Technological Research, Polish Academy of Sciences
ul. Pawinskiego 5B, 02-106 Warsaw, Poland
e-mail: tzielins@ippt.pan.pl

Abstract

Acoustics of stiff porous media with open porosity can be very effectively modelled using the so-called Johnson-Champoux-Allard-Pride-Lafarge model for sound absorbing porous media with rigid frame. It is an advanced semi-phenomenological model with eight parameters, namely: the total porosity, the viscous permeability and its thermal analogue, the tortuosity, two characteristic lengths (one specific for viscous forces, the other for thermal effects), and finally, viscous and thermal tortuosities at the frequency limit of 0Hz. Most of these parameters can be measured directly, however, to this end specific equipment is required different for various parameters. Moreover, some parameters are difficult to determine. This is one of several reasons for the so-called multiscale approach where the parameters are computed from specific finite-element analyses based on some realistic geometric representations of the actual microstructure of porous material. Such approach is presented and validated for layers made up of loosely-packed small identical rigid spheres. The sound absorption of such layers was measured experimentally in the impedance tube using the so-called two-microphone transfer function method. The layers are characterised by open porosity and semi-regular microstructure: the identical spheres are loosely packed by random pouring and mixing under the gravity force inside the impedance tubes of various size. Therefore, the regular sphere packings were used to generate Representative Volume Elements suitable for calculations at the micro-scale level. These packings involve only one, two or four spheres so that the three-dimensional finite-element calculations specific for viscous, thermal, and tortuous effects are feasible. In the proposed geometric packings the spheres were slightly shifted in order to achieve the correct value of total porosity which was precisely estimated for the layers tested experimentally. Finally, in this paper some results based on the self-consistent estimates are also provided.

Key words: sound absorption, porous materials, multiscale modelling, microstructure.

I. INTRODUCTION

Assemblies of rigid spheres form porous media where the air fills the space between the spheres which constitute a rigid frame. An important feature of all even tightly-set packings of (identical) spheres is that they create granular media with fully-open porosity. The energy of acoustic waves which penetrate such porous granular media can be significantly dissipated because of an interaction of the vibrating air particles with the surface of small rigid motionless spheres. Models for sound absorbing rigid-frame porous media are therefore suitable for description and quantitative estimation of this phenomenon. On the other hand, the layers of small rigid spheres are suitable to test how microstructure of porous media affects its absorptive properties, and also to validate the so-called multi-scale modelling applied to this classic problem of poro-acoustics, as well as some simple or more complex propositions for microstructure representations.

There are many macroscopic models for sound absorbing porous or fibrous materials. For quite a long time they were rather simple empirical models involving only a couple of material parameters. In consequence such models often impose some restrictive requirements (like, for example, high porosity) or limitations with respect to the valid frequency range. Such are, for example, the purely empirical models proposed by Delany and Bazely[1] for fibrous materials and later significantly improved by Miki[2,3]. Empirical models for rigid frame porous materials are still being proposed (see, for example, models by Voronina[4,5]), however, a semi-phenomenological model which involves more physical insight was established in 1990s basing on achievements and previous publications of many researchers. It is the so-called Johnson-Champoux-Allard model[6–11] or its tuned-up versions with enhancements proposed by Pride[12,13] or Lafarge[14]. Recently, the acoustic wave propagation in macroscopically inhomogeneous materials using the equivalent fluid approach was also studied by Cieszko et al.[15].

In general, acoustics of granular media with open porosity can be modelled in the same or very similar way as other porous or fibrous materials. For example, Attenborough[16] proposed a model that predicts the acoustical characteristics of rigid fibrous absorbents and granular materials from five parameters (porosity, flow resistivity, tortuosity, steady flow shape factor, and dynamic shape factor). Later, this author examined also the slow acoustic wave in air-filled granular media[17] with respect to the predictions given by the classical theory of rigid porous medium and the rigid-frame limit provided by the model based on the Biot theory of poroelasticity. An empirical model proposed by Voronina and Horoshenkov[18] for loose granular materials allows for evaluation of their acoustic performance with respect to only four parameters: the characteristic particle dimension, porosity, tortuosity and specific density of the grain base. Horoshenkov and Swift[19] applies a simple model for the prediction of the acoustic properties of porous granular media with some assumed pore geometry and pore size distribution close to log-normal. The model is based on the rational Padé approximation approach[20].

Porous media made up of fused glass beads were studied experimentally by Charlaix et al.[21] with respect to the crucial (for poroacoustics) characteristics of dynamic permeability. They measured the dynamic permeability on samples of glass beads (also on crushed glass) slightly sintered together. Beads of three different mean diameters were used, namely, 1.7 mm, 0.95 mm, and 0.5 mm, with a variation of roughly 20% around that mean, and the frequency range was from 0.1 Hz to 1 kHz.

Chapman and Higdon[22] addressed the problem of oscillatory Stokes flow in periodic porous media, considering the consolidated media composed from spheres arranged in three classic lattices: simple cubic (SC), body centered cubic (BCC) and face centered cubic (FCC). Detailed results of the dynamic permeability computed mainly for closely packed concentrations are compared with previously published results.

More complete results concerning sound propagation and absorption in air-saturated random packings of beads were provided by Allard et al.[23]. These authors measured a layer of (nearly) identical glass beads of diameter 1.46 mm ($\pm$0.02 mm) in a Kundt tube, and the measured normalised surface acoustic impedance at normal incidence of the layer of thickness 5.2 cm was compared with the prediction calculated from the Johnson-Champoux-Allard model (of the equivalent fluid). To this end, the necessary macroscopic parameters for random packings of glass beads having a quasi-uniform diameter were first measured with nonacoustical and acoustical methods. Thus, for example, the measured porosity was 0.4 like in the case of random loose packings of identical beads[24,25], and the measured (viscous) permeability was 1.5×10^{-9} m^2. Tortuosity evaluated from conductivity measurements was 1.37. Also the normalized compressibility (of the equivalent fluid) measured using the Tarnow method[26], and the squared ratio of the speed of sound in air to the frequency-dependent effective speed of sound of equivalent fluid were compared with model predictions.

Umnova et al.[27] proposed analytical expressions for dynamic and static permeability, high-frequency limit of tortuosity, and the characteristic viscous dimension in porous media composed of packings of spheres derived using a cell model (based of the simple cubic lattice) with an adjustable cell radius which allows for hydrodynamic interactions between the spherical particles; the other parameters are: the volume porosity and the particle radius. It is shown that better results are obtained for the cell radius corresponding to that of the sphere circumscribing a unit cell of a cubic lattice arrangement. The results are compared with some numerical data published previously by Chapman and Higdon[22], Allard et al.[23], or Charlaix et al.[21].

The work by Gasser at el.[28] is one of the first where the sound absorption of rigid porous media (made up of identical rigid spheres) is calculated from microstructure using the finite element method. The regular face centered cubic (FCC) packing of rigid spheres was assumed with porosity 26%. The parameters of tortuosity and the dynamic length were obtained by solving a potential flow, whereas a steady viscous flow was used to compute the permeability. These parameters allowed use the approximation formulas for the frequency-dependent effective density. Similarly, the frequency-dependent effective compressibility was also determined on the basis of macroscopic parameters calculated from the microscopic finite element model. In the paper the radius of the spheres was 1 mm, and a soldering neck of radius 0.15 mm binding them together was taken into account. Thus, the variations of characteristic lengths (thermal and viscous) were shown as functions of the normalized sintered neck radius for different neck descriptions, as well as the tortuosity parameter versus neck radius for cylindrical necks. The work was purely numerical, however, some comparison with experimental results of the literature is provided.

The microostructure-based approach for modelling of porous media is applied by Perrot et al.[29,30] for open-cell aluminium foams and more recently for polymeric foams[31]. It was also demonstrated that two-dimensional microostructure-based modelling of sound absorbing fibrous material may be useful for optimisation of the cross section of rigid solid fibres[32]. Another two-dimensional microostructure-based analyses allowed Cortis and Berryman[33] to correctly describe dynamic viscous flow in channels with (fractal) rough surfaces which limits the application of classical approximation models for sound absorbing porous media. Chevillotte et al.[34] used microstructure-based model for sound absorption predictions of perforated closed-cell metallic foams. Recently, Chevillotte, Perrot, and Guillon[35] studied a link between microstructure and acoustical macro-behavior of double porosity foams. Hoang and Perrot[36] investigated porous microstructure for local characteristic lengths governing sound wave properties in solid foams. Boutin and Geindreau[37] used the homogenization of periodic media and the self-consistent method to derive three estimates and also exact bounds of dynamic permeability in granular media. More recently, they used also the same approach to study dynamic and thermal permeability, diffusion and trapping constant through porous media represented by sphere and polyhedron packings[38].

In 2009 the microstructure-based modelling of porous materials was also applied by Lee, Leamy and Nadler[39] for the problem of sound propagation in granular media of rigid spheres. These authors used regular, close packings of spheres as microstructural geometry representations to compare between the so-called direct and hybrid numerical approach. Since both approaches utilised the same Representative Volume Elements the direct and hybrid results were nearly identical. The numerical calculations by authors were also confronted with the results found in literature.

The present paper follows up the proceeding used by Lee et al.[39] and in some other works mentioned above. The hybrid microstructure-based modelling is applied for the problem of sound absorption in granular media composed of randomly (or semi-randomly) packed rigid spherical beads. To this end, regular sphere packings are used, however, the spheres are not closely-packed, yet they are slightly shifted apart or, on the contrary, a minor overlapping is allowed. Such approach permits to use rather simple geometries to represent the porous microstructure in finite-element analyses, and is validated by the results of original experimental tests carried out by the author.

The paper is organised as follows. First, the experimental tests of sound absorption by layers made up of identical rigid plastic beads are reported. Next, three types of Representative Volume Elements (RVEs) are proposed and examined. Then, the multi-scale modelling is discussed and the hybrid approach using three RVEs is applied for microstructure-based modelling of the considered problem. In this context, also some self-consistent estimates based on a bicomposite spherical cell are provided. Finally, the microstructure-based calculations and the self-consistent estimates are compared with some of the results of experimental tests.

II. TESTING FREELY-PACKED LAYERS OF BEADS

A series of acoustical tests was carried out in the impedance tube on layers composed of identical rigid spherical beads. The diameter of each sphere was 5.9 mm and the layers were prepared in the following way:

- First, a quantity of beads was freely poured into the testing tube set in vertical position.
- Then, the tube was being shaken (manually) in order to stably pack the beads.
- Occasionally, the top layer of beads was softly clapped with a flat piston to level its surface.

It was found that the described proceeding gave always stable microstructure and excellent repeatability of measurements. On the other hand, the arrangements of spheres were constrained by the tube walls (see Figure 1) so that even long mechanical mixing would never result in close packing (especially in case the smallest tube). Such semi-randomly packed layers of rigid beads were tested in the impedance tube (see Figure 2) using the technique based on the two-microphone transfer function method[40,41]. In that way the surface acoustic impedance and sound absorption was measured for each layer. As a matter of fact, the tests were carried out in three vertically-positioned tubes of various diameter (see Figures 1 and 2), namely: in a large tube with diameter of 100 mm, in a medium tube with diameter of 63.5 mm, and in a small tube with diameter 29 mm. Depending on the tube diameter

Figure 1: Randomly-packed spherical beads inside three tubes of various size

Figure 2: Three vertically-positioned impedance tubes

Table I: Freely-packed layers of spherical beads in impedance tubes of various size

Tube size:	**Large**	**Medium**		**Small**		
Tube diameter:	100 mm	63.5 mm		29 mm		
Frequency range:	50–1600 Hz	100–3200 Hz		500–6400 Hz		
Layer symbol:	**L-41**	**M-41**	**M-106**	**S-41**	**S-106**	**S-200**
Layer height:	41 mm	41 mm	106 mm	41 mm	106 mm	200 mm
Number of beads:	1840	708	1840	147	380	710
Porosity:	**∼ 39%**	**∼ 41%**		**∼ 42%**		

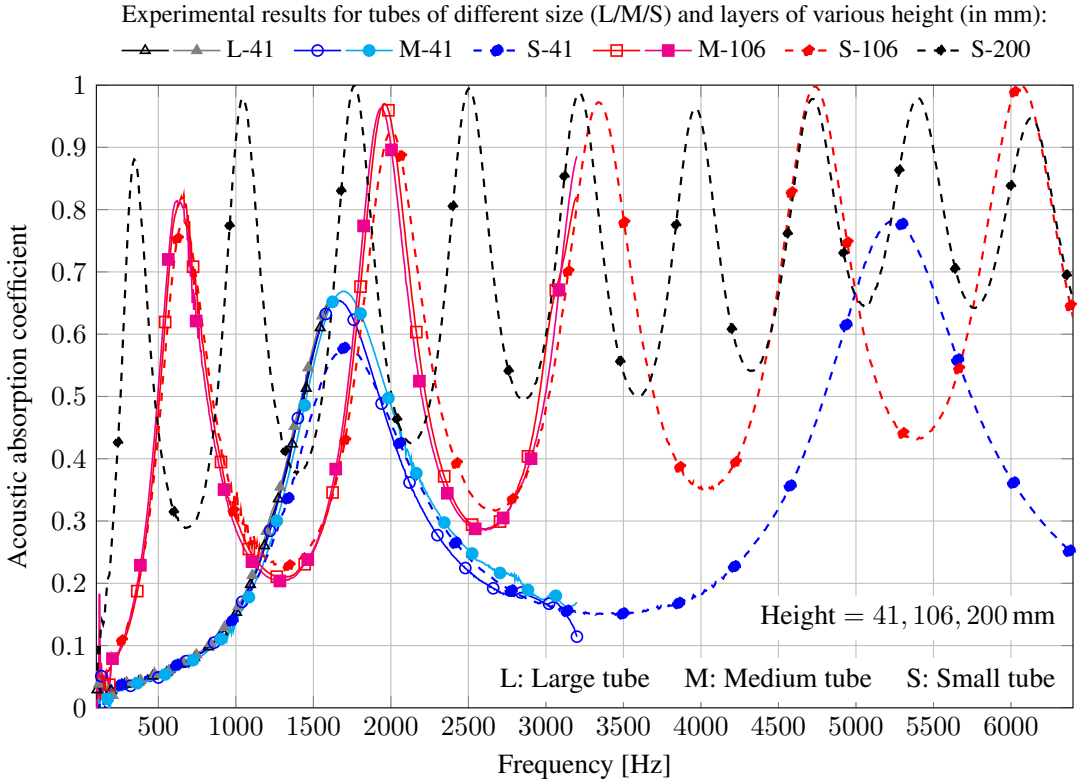

Figure 3: Acoustic absorption of freely-packed beads – experimental results

the measurements were in frequency range: from 50 Hz to 1.6 kHz for the large tube, from 100 Hz to 3.2 kHz for the medium tube, and from 500 Hz to 6.4 kHz in case of the small tube.

Each cylindrical layer had a certain height which was thoroughly measured, so that the total volume of layer could be calculated as the product of the layer's height and the cross-section area of the tube. Moreover, the beads from each layer were weighted together so that their total number could be approximately determined, basing on the fact that the mass of a single bead is 0.3 g; knowing the spherical bead's volume, the total volume of all beads in a particular layer could be estimated. That result together with the total volume of cylindrical layer allowed to estimate the solid-phase volume and then the layer's porosity. All those data are summarised in Table I for 6 particular layers.

In case of the large tube all beads (approximately 1840 of them) formed a layer 41 mm in height with the estimated porosity of 39%. In case of the medium tube, only about 708 beads were necessary to form the 41 mm-high layer; since the packing could not be so dense, the porosity was approximately 41%. The whole assembly of 1840 spherical beads formed in the medium tube a layer of similar porosity and 106 mm in height. Eventually, the 41 mm-high and 106 mm-high layers were formed in the small tube using estimated numbers of 147 or 380 beads, respectively. The porosity was approximately 42% in both cases. A very similar porosity was obtained when approximately 710 beads were poured and mixed in the small tube to form a layer of 200 mm in height.

It must be emphasized that roughly the same correspondence of the cylindrical layer's porosity with respect to its height and diameter were achieved for independent pouring and mixing of rigid beads into the tubes. This was also confirmed by the excellent repeatability and good accordance of the results of independent experimental tests carried out in the impedance tubes. These results are presented in Figure 3 where the frequency-varied curves of the acoustic absorption coefficient are shown for all 6 sample-layers discussed above. For each of the layers measured in the large and medium tubes two independent measurements are shown to illustrate the test repeatability. Moreover, quite a good accordance is found (in the common frequency range) between the samples tested in tubes of different diameter; some obvious discrepancies (compare the curves S-106 with M-106, or S-41 with M-41 and L-41 in Figure 3) – visible especially when referring to the results form the small tube which diameter is only less than five times bigger than the size of beads – are because of different porosity and irregularities in the packing constrained by the sides of the tube.

Figure 3 shows only the testing results of porous layers. In further Sections these experimental curves will be compared with the acoustic absorption calculated from the advanced multi-scale modelling – discussed in the previous Section – which should involve several finite-element analyses based on some three-dimensional geometries more or less representative for the porous medium microstructure.

III. PERIODIC SPHERE PACKINGS AND REPRESENTATIVE VOLUME ELEMENTS

In order to apply the microstructure-based approach to modelling of the porous layers tested in the previous Section, one needs some representative models of their micro-geometry. Moreover, the representative micro-geometric cells should be periodic to satisfy some mathematical requirements of the discussed multi-scale modelling. Since the layers are made up of identical rigid spherules it seems reasonable to start up with regular, periodic sphere packings as the base for the micro-geometric representations. Three sphere packings known very well, for example, from crystallography lattices, will be considered, namely:

- **Simple Cubic (SC)** – the spheres are arranged at the corners of the cubic cell; there is only 1 sphere per unit cell,
- **Body Centered Cubic (BCC)** – the spheres are arranged at the corners of the cubic cell with another sphere at the cube centre; there are 2 spheres per unit cell,
- **Face Centered Cubic (FCC)** – the spheres are arranged at the corners and centre of each face of the cubic cell; there are 4 spheres per unit cell.

Spheres are closely-packed in their cells when the sphere diameter and the cell egde length are in some definite proportion so that the rigid spheres forming one of the above type of arrangement are in full contact. These proportions together with some other data are listed in Table II for the packing types SC, BCC, and FCC. The ratio of sphere volume to unit cell volume is also strictly definite and for closely-packed arrangements it is 0.524 for SC, 0.68 for BCC, and 0.74 for FCC, which means that the void space in unit cell (or the porosity) is 47.6%, 32%, and 26%, respectively.

Table II: Geometric data for periodic RVEs obtained from three regular close sphere packings

Packing type:	**SC**	**BCC**	**FCC**
number of spheres:	1	2	4
edge to diameter ratio:	1	$\frac{2}{\sqrt{3}} = 1.155$	$\sqrt{2} = 1.414$
edge length* [mm]:	5.90	6.81	8.34
solid volume fraction:	$\frac{\pi}{6} = 0.524$	$\frac{\pi\sqrt{3}}{8} = 0.680$	$\frac{\pi\sqrt{2}}{6} = 0.740$
porosity [%]:	**47.6**	**32.0**	**26.0**

*for the sphere diameter 5.9 mm

In practice, although, the spherical beads tend to be identical their distribution is usually not so regular as in case of the presented periodic arrangements, because of random pouring and tube constraints. It has been shown in the previous Sections that in case of random packing, that is, when the spheres are dropped or packed manually, the porosity is about 39 to 41% or even slightly higher, about 42% when the free packing of spheres is somehow constrained by the sides of container which is only a few times bigger their size. This is, however, far more superior than the porosity of BCC or FCC arrangements which are densely packed, yet at the same time significantly smaller than the porosity of SC packing.

Total porosity is an extremely important parameter for models predicting the sound propagation and absorption in porous media, therefore, it seems reasonable that it should be exactly represented by the micro-geometric model. Now, the regular periodic sphere packings will be used to model the experiment described in the previous Section, though, obviously they should be somehow adjusted in order reflect the total porosity. To this end, the SC packing must be compressed so that the rigid spheres overlap, whereas in case of the BCC and FCC packings the spheres must be slightly spread apart.

The closely-packed arrangements of spheres are shown in Figure 4 for packing types SC, BCC, and FCC, that is, with cubic cells. Notice that in case of the BCC arrangement the cube is vertically shifted by half its length, so that the "body centered" sphere appears on top and bottom faces (and not inside the cube as in commonly used representation). The corresponding periodic cells of Representative Volume Elements are presented in the top row of Figure 5 for closely-packed arrangements, and in the bottom row of Figure 5 for arrangements slightly compressed (SC) or spread

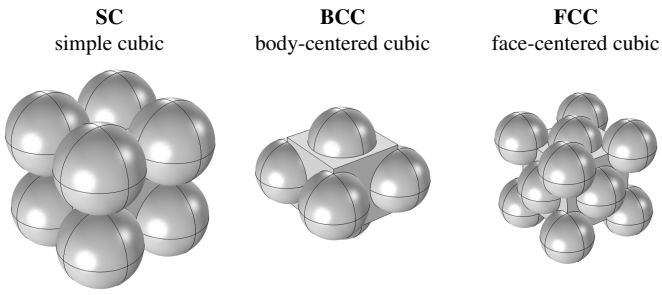

Figure 4: Regular closely-packed arrangements of spheres

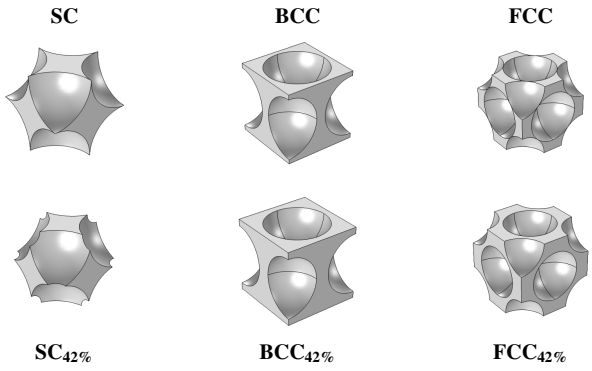

Figure 5: Represtative Volume Elements (RVEs) obtained from the regular sphere packings

Table III: Geometric data of three porosity-adjusted periodic RVEs

Packing type:	**$SC_{42\%}$**	**$BCC_{42\%}$**	**$FCC_{42\%}$**
number of spheres:	1	2	4
edge to diameter ratio:	0.960	1.218	1.534
edge length* [mm]:	5.66	7.19	9.05
by shifting spheres the porosity is set to 42%			

*for the sphere diameter 5.9 mm

(BCC, FCC) so that the total porosity would be 42%, that is, in agreement with the value found experimentally. These arrangements with regularly shifted spheres will be now referred as $SC_{42\%}$, $BCC_{42\%}$, and $FCC_{42\%}$. Table III presents some relevant geometric data corresponding to these RVEs, for example, their size assuming that the sphere diameter is 5.9 mm (which is the very diameter of the spherical beads used in experimental tests). Notice that the representative cell with simple cubic packing has been diminished within the process of porosity adjustment, whereas the cells with body centered cubic and face centered cubic packings are slightly enlarged with respect to their closely-packed originals.

IV. MULTI-SCALE ANALYSIS

A. Effective density, bulk modulus, and speed of sound

Multi-scale asymptotic modelling is a homogenisation technique suitable for analysis of vibrations and wave propagation in non-homogeneous media[42], in particular, for porous media saturated with a fluid. It can be shown that in case of acoustic waves, two main phenomena responsible for their absorption and propagation, that is, the viscous and thermal effects are uncoupled, because at the micro-scale the (oscillating) flow is incompressible; therefore, they were often studied separately. In this Section the multi-scale analyses for both effects will be discussed at limiting cases of very low and very high frequencies suitable for the hybrid approach.

Dynamic behaviour of porous medium saturated by a viscous fluid was studied for example by Auriault et al.[43,44] or Johnson et al.[6] and many others. More recently multi-scale numerical analyses carried out by Cortis et al.[33,45] showed that the pore roughness affects the dynamic permeability at high-frequencies. The influence of rigid structure of pores on wave-propagation in a porous-medium was also studied by Cieszko et al.[46]. Thermal effects with respect to sound propagation were thoroughly investigated for example by Lafarge[14], who also gave a complete multi-scale description of the problem of sound propagation and absorption in a rigid porous medium[47]. Macroscopic formulas can also be found in the book by Allard and Atalla[10].

From the macroscopic perspective the fluid-equivalent approach is applied where a rigid porous medium is substituted by an effective fluid characterised by the effective density and bulk modulus, and eventually, by the effective speed of sound. As a matter of fact, these quantities vary with frequency since porous media are dispersive. It is rather obvious to relate the frequency-dependent function of effective density $\varrho_\mathrm{e}(\omega)$ to the constant density of actual fluid in pores ϱ_f, therefore:

$$\varrho_\mathrm{e}(\omega) = \frac{\varrho_\mathrm{f}\alpha(\omega)}{\phi}\,. \tag{1}$$

Here, $\alpha(\omega)$ is the so-called dynamic (viscous) tortuosity. It is a complex-valued function of frequency. Its real part is always greater than 1, since it describes the apparent increase of the density because of visco-inertial interaction with the solid skeleton.

Similarly, the effective bulk modulus of equivalent fluid $K_\mathrm{e}(\omega)$ is related to the bulk modulus of pore-fluid K_f, as follows

$$K_\mathrm{e}(\omega) = \frac{K_\mathrm{f}}{\phi\beta(\omega)}\,, \tag{2}$$

where $\beta(\omega)$ is the compressibility ratio, that is, the ratio of the effective compressibility $1/K_\mathrm{e}(\omega)$ to the pore-fluid compressibility $1/K_\mathrm{f}$. It was shown that this complex and frequency-dependent function can be expressed by the following formula

$$\beta(\omega) = \gamma - \frac{\gamma-1}{\alpha'(\omega)} \tag{3}$$

where γ is the ratio of specific heats of pore-fluid, whereas $\alpha'(\omega)$ is the so-called thermal dynamic tortuosity (an analogue of its viscous predecessor).

Now, it is easy to show that the dimensionless functions $\alpha(\omega)$ and $\beta(\omega)$ are necessary to calculate the effective speed of sound in fluid equivalent porous medium:

$$c_\mathrm{e}(\omega) = \sqrt{\frac{K_\mathrm{e}(\omega)}{\varrho_\mathrm{e}(\omega)}} = \frac{c_\mathrm{f}}{\sqrt{\alpha(\omega)\beta(\omega)}}\,, \tag{4}$$

where $c_\mathrm{f} = \sqrt{K_\mathrm{f}/\varrho_\mathrm{f}}$ is the speed of sound in the actual fluid which fills the pores. When this complex-valued frequency-dependent characteristics $c_\mathrm{e}(\omega)$ is determined, it can be used by the Helmholtz equation for time-harmonic acoustics.

B. Dynamic tortuosities and macroscopic parameters

At each frequency ω the viscous dynamic tortuosity $\alpha(\omega)$ is inversely proportional to the so-called dynamic (viscous) permeability of porous medium $\widehat{k}(\omega)$ studied by many authors (it is a generalisation of the classic static permeability), namely

$$\alpha(\omega) = \frac{\phi\nu}{\mathrm{i}\omega\,\widehat{k}(\omega)}\,. \tag{5}$$

Here, ϕ is the (open) porosity of porous material, while $\nu = \mu/\varrho_\mathrm{f}$ is the kinematic viscosity of fluid in pores with μ being its (dynamic) viscosity. Now, it should be noticed that the thermal dynamic tortuosity $\alpha'(\omega)$ was is fact introduced by the analogy to the above formula since it is equal

$$\alpha'(\omega) = \frac{\phi\nu'}{\mathrm{i}\omega\,\widehat{k'}(\omega)} \tag{6}$$

where $\nu' = \nu/\mathrm{Pr}$, with Pr being the Prandtl number for the fluid in pores, while $\widehat{k'}(\omega)$ is a thermal analogue of viscous dynamic permeability, introduced by Lafarge[14,47].

It is clearly visible from the formulas presented in the previous section that the two dynamic tortuosities are necessary to determine the effective speed of sound for porous medium which can be then substituted in modelling by the corresponding equivalent fluid. The Johnson-Champoux-Allard model[10] and its enhanced versions propose some analytical, semi-phenomenological yet rather precise approximations for these tortuosity functions.

Both dynamic tortuosities depend on the geometry of solid structure of porous medium as well as on the saturating fluid. In order to calculate the viscous dynamic tortuosity function from the formulas of the Johnson-Champoux-Allard-Pride-Lafarge model[10,11] one needs to know the kinematic viscosity ν of fluid in pores, and five purely geometrical parameters which macroscopically characterise the solid (rigid) frame of porous medium, namely: its porosity ϕ, the tortuosity factor α_∞, the static permeability $\widehat{k}_0$, the viscous characteristic length Λ, and the viscous static tortuosity (i.e, at 0 Hz) α_0. To determine the thermal dynamic tortuosity function the kinematic viscosity ν and Prandtl number Pr of fluid in

pores are necessary (or, as a matter of fact, their ratio $\nu' = \nu/\mathrm{Pr}$), and moreover, four macroscopic parameters resulting exclusively from the porous geometry: the porosity ϕ, the thermal analogue of static permeability $\widehat{k}'_0$, the characteristic length for thermal effects Λ', and the thermal static tortuosity (i.e, at 0 Hz) α'_0. In total, there are 8 macroscopic parameters which depend (only) on the geometry of rigid structure of porous medium. All of them can be calculated from the microstructure of porous medium by solving the corresponding Boundary-Value Problems (BVPs) discussed below. For each of these problems, it is assumed that the representative cell of porous medium is periodic and that the problems are defined on the fluid domain Ω_f with specific boundary conditions set on the solid walls, i.e., on the solid-fluid interface $\partial\Omega_\mathrm{sf}$, and relevant periodic boundary conditions set on the corresponding fluid parts of cell faces. Finally, the averaging operator $\langle\ldots\rangle_\mathrm{f} = \frac{1}{\Omega_\mathrm{f}}\int_{\Omega_\mathrm{f}}(\ldots)dV$ means averaging over the fluid domain, and since the rigid solid does not contribute the average over the whole cell equals $\frac{1}{\Omega}\int_\Omega(\ldots)dV = \phi\langle\ldots\rangle_\mathrm{f}$, where ϕ is the porosity.

C. Electric conduction problem

The classical tortuosity of porous medium α_∞ is in fact the limit of the real part of the frequency-dependent dynamic tortuosity function $\alpha(\omega)$ for the frequency reaching infinity, $\omega \to \infty$. In such high-frequency regime the viscosity of fluid can be neglected and its behaviour tend to be as for the perfect fluid. The resistance of flow through porous medium is therefore purely inertial.

It can be shown that the problem of incompressible perfect fluid flow coincides formally with the electrical problem of a porous medium made up of electrically insulating solid filled with a conductive fluid[47–50]. By applying a unit electric field $\underline{\boldsymbol{e}}^{(m)}$, that is a constant and dimensionless vector field acting uniformly in some direction direction m in the whole fluid domain, the microscopic scaled current in the saturating fluid will be

$$\underline{\boldsymbol{j}} = \sigma_\mathrm{f}\underline{\boldsymbol{E}}^{(m)}\,, \tag{7}$$

where σ_f is the fluid electric conductivity, and $\underline{\boldsymbol{E}}^{(m)}$ is the scaled, i.e., dimensionless, electric field (it is as a matter of fact, the local electric field divided by the applied macroscopic electric potential gradient). The macroscopic current is by definition the average of $\underline{\boldsymbol{j}}$ over the porous medium and equals

$$\underline{\boldsymbol{J}} = \phi\left\langle\underline{\boldsymbol{j}}\right\rangle_\mathrm{f} = \phi\sigma_\mathrm{f}\left\langle\underline{\boldsymbol{E}}^{(m)}\right\rangle_\mathrm{f}. \tag{8}$$

It obeys a macroscopic Ohm's law:

$$\underline{\boldsymbol{J}} = \underline{\underline{\boldsymbol{\sigma}}}_\mathrm{e}\cdot\underline{\boldsymbol{e}}^{(m)}\,, \tag{9}$$

where $\underline{\underline{\boldsymbol{\sigma}}}_\mathrm{e}$ is the second-order tensor of effective (homogenized, macroscopic) conductivity of porous medium. It is linearly related to the electric conductivity of fluid in pores σ_f and this relation is determined by the tortuosity factor of porous medium. In that way, the second-order tortuosity tensor can be introduced, namely

$$\underline{\underline{\boldsymbol{\alpha}}}_\infty = \phi\sigma_\mathrm{f}\,\underline{\underline{\boldsymbol{\sigma}}}_\mathrm{e}^{-1}. \tag{10}$$

As a matter of fact, these observations allow to measure the tortuosity factor experimentally, provided that the solid structure of porous medium is made up from dielectric material. Then, it can be filled with a conductive fluid and from the measurements of electric current induced in the porous sample by application of a uniform electric field the effective conductivity can be found, which allows to calculate the tortuosity from the above formula, if the electric conductivity of fluid and the total porosity are known.

Using formulas (8), (9) and (10) the following relation is obtained

$$\underline{\boldsymbol{e}}^{(m)} = \underline{\underline{\boldsymbol{\alpha}}}_\infty\cdot\left\langle\underline{\boldsymbol{E}}^{(m)}\right\rangle_\mathrm{f}, \tag{11}$$

from which the the components of the inverse tortuosity tensor can be easily derived

$$\alpha^{-1}_{\infty(mn)} = \left(\underline{\underline{\boldsymbol{\alpha}}}_\infty^{-1}\cdot\underline{\boldsymbol{e}}^{(m)}\right)\cdot\underline{\boldsymbol{e}}^{(n)} = \left\langle\underline{\boldsymbol{E}}^{(m)}\right\rangle_\mathrm{f}\cdot\underline{\boldsymbol{e}}^{(n)}. \tag{12}$$

It means that the tortuosity tensor can be determined when the scaled electric fields $\underline{\boldsymbol{E}}^{(m)}$ are known for three different (orthogonal) directions m of the unit vector fields $\underline{\boldsymbol{e}}^{(m)}$. And to this end, three electric conductivity problems must be solved in a representative periodic cell of porous medium.

The scaled problem of electric conduction of porous cell means that for a constant (i.e, uniform in the fluid domain) unit vector field $\underline{\boldsymbol{e}}^{(m)}$ the sought microscopic field $\underline{\boldsymbol{E}}^{(m)}$ must be equal

$$\underline{\boldsymbol{E}}^{(m)} = \underline{\boldsymbol{e}}^{(m)} - \nabla\, q_{(m)} \quad \text{in } \Omega_\mathrm{f}\,, \tag{13}$$

where $q_{(m)}$ is an unknown potential field periodic on Ω_f, in fact $-\nabla\, q_{(m)}$ is a fluctuating part of $\underline{\boldsymbol{E}}^{(m)}$, which therefore must satisfy the divergence-free condition, namely,

$$\nabla\cdot\underline{\boldsymbol{E}}^{(m)} = 0 \quad \text{in } \Omega_\mathrm{f}\,, \tag{14}$$

and also the boundary condition on the insulating solid walls (i.e., the solid-fluid interface)

$$\underline{\boldsymbol{E}}^{(m)}\cdot\underline{\boldsymbol{n}} = 0 \quad \text{on } \partial\Omega_\mathrm{sf}, \tag{15}$$

where $\underline{\boldsymbol{n}}$ is the unit vector normal to the interface.

Eventually, the electric conduction problem can be reduced to the Laplace problem for the unknown (scaled electric) potential field $q_{(m)}$ periodic on Ω_f, namely, in the fluid domain

$$\triangle\, q_{(m)} = 0 \quad \text{in } \Omega_\mathrm{f}\,, \tag{16}$$

and on the solid walls

$$\nabla q_{(m)}\cdot\underline{\boldsymbol{n}} = \underline{\boldsymbol{e}}^{(m)}\cdot\underline{\boldsymbol{n}} \quad \text{on } \partial\Omega_\mathrm{sf}. \tag{17}$$

When the potential field $q_{(m)}$ is found the scaled electric field $\underline{\boldsymbol{E}}^{(m)}$ is computed from the formula (13).

Now, the formula for the components of the inverse tensor of tortuosity (12) can be transformed as follows

$$\begin{aligned}\alpha^{-1}_{\infty(mn)} &= \left\langle\underline{\boldsymbol{E}}^{(m)}\cdot\underline{\boldsymbol{e}}^{(n)}\right\rangle_\mathrm{f}\\ &= \left\langle\underline{\boldsymbol{E}}^{(m)}\cdot\underline{\boldsymbol{E}}^{(n)}\right\rangle_\mathrm{f} + \left\langle\underline{\boldsymbol{E}}^{(m)}\cdot\nabla q_{(n)}\right\rangle_\mathrm{f}.\end{aligned} \tag{18}$$

The last term in this expression vanishes (by integration by parts), because the electric field is divergence-free in the compact fluid domain, Eq. (14), and satisfies the boundary condition (15) on the solid walls. Therefore, the components of the tortuosity tensor can be computed from the following formula

$$\alpha_{\infty(mn)} = \frac{1}{\left\langle\underline{\boldsymbol{E}}^{(m)}\cdot\underline{\boldsymbol{E}}^{(n)}\right\rangle_\mathrm{f}}, \tag{19}$$

which explicitly shows the symmetry of this tensor.

When the system of reference coincides with the principal axes of a tensor, its matrix representation reduces to the diagonal form; thus, in case of the tortuosity tensor, its components are

$$\alpha_{\infty(mn)} = \alpha_{\infty(m)}\,\delta_{mn}\,, \tag{20}$$

where $\alpha_{\infty(m)}$ are the principal values (eigenvalues) of the tortuosity tensor and δ_{mn} is the Kronecker's delta. (Here and below no summation is imposed on any indices.) Moreover, in the principal axes system the mean scaled electric field is colinear to the vector $\underline{\boldsymbol{e}}^{(m)}$ in the following way

$$\left\langle \underline{\boldsymbol{E}}^{(m)} \right\rangle_{\mathrm{f}} = \alpha_{\infty(m)}^{-1}\,\underline{\boldsymbol{e}}^{(m)}\,, \tag{21}$$

which also means that

$$\left\langle \underline{\boldsymbol{E}}^{(m)} \right\rangle_{\mathrm{f}} \cdot \left\langle \underline{\boldsymbol{E}}^{(m)} \right\rangle_{\mathrm{f}} = \alpha_{\infty(m)}^{-2}\,. \tag{22}$$

All this eventually leads to the following expressions for the principal components of tortuosity tensor

$$\begin{aligned} \alpha_{\infty(m)} &= \frac{1}{\left\langle \underline{\boldsymbol{E}}^{(m)} \right\rangle_{\mathrm{f}} \cdot \underline{\boldsymbol{e}}^{(m)}} \\ &= \frac{1}{\left\langle \underline{\boldsymbol{E}}^{(m)} \cdot \underline{\boldsymbol{E}}^{(m)} \right\rangle_{\mathrm{f}}} = \frac{\left\langle \underline{\boldsymbol{E}}^{(m)} \cdot \underline{\boldsymbol{E}}^{(m)} \right\rangle_{\mathrm{f}}}{\left\langle \underline{\boldsymbol{E}}^{(m)} \right\rangle_{\mathrm{f}} \cdot \left\langle \underline{\boldsymbol{E}}^{(m)} \right\rangle_{\mathrm{f}}}\,. \end{aligned} \tag{23}$$

In case of isotropy of porous medium, the flows or scaled electric fields $\underline{\boldsymbol{E}}^{(m)}$ caused by the unit-gradient vector fields $\underline{\boldsymbol{e}}^{(m)}$ will be identical for any direction m, and the tortusosity tensor is characterised by the unique scalar constant α_∞, namely,

$$\underline{\underline{\boldsymbol{\alpha_\infty}}} = \alpha_\infty \underline{\underline{\boldsymbol{I}}}\,, \quad \text{where} \quad \alpha_\infty = \alpha_{\infty(m)}\,. \tag{24}$$

The scalar parameter of tortuosity may also be used when the propagation is simply considered along the direction m defined by the unit vector $\underline{\boldsymbol{e}}^{(m)}$.

Using the solution for the electric conduction problem of periodic representative cell of porous medium, the viscous characteristic length can be also determined as follows

$$\Lambda = 2\frac{\displaystyle\int_{\Omega_{\mathrm{f}}} \underline{\boldsymbol{E}}^{(m)} \cdot \underline{\boldsymbol{E}}^{(m)} dV}{\displaystyle\int_{\partial\Omega_{\mathrm{sf}}} \underline{\boldsymbol{E}}^{(m)} \cdot \underline{\boldsymbol{E}}^{(m)} dS}\,. \tag{25}$$

Its thermal counterpart is calculated directly form the porous geometry as the doubled ratio of the volume of fluid domain to the surface of solid walls (i.e., the solid-fluid interface):

$$\Lambda' = 2\frac{\displaystyle\int_{\Omega_{\mathrm{f}}} dV}{\displaystyle\int_{\partial\Omega_{\mathrm{sf}}} dS}\,. \tag{26}$$

D. Viscous flow problem

In a static regime or at very low frequencies, when $\omega \to 0$, the viscous effects dominate over the inertial ones. The fluid flow through a periodic cell is described by the microscopic fields of velocity $\underline{\boldsymbol{v}}$ and pressure p, both periodic over the cell's fluid domain. They must satisfy the Stokes equations of steady-state viscous flow, namely,

$$\mu\triangle\underline{\boldsymbol{v}} - \nabla p = \underline{\boldsymbol{g}} \quad \text{in } \Omega_{\mathrm{f}}, \tag{27}$$

and

$$\nabla \cdot \underline{\boldsymbol{v}} = 0 \quad \text{in } \Omega_{\mathrm{f}}, \tag{28}$$

with no-slip boundary conditions on solid walls (i.e., the solid-fluid interface):

$$\underline{\boldsymbol{v}} = \underline{\boldsymbol{0}} \quad \text{on } \partial\Omega_{\mathrm{sf}}. \tag{29}$$

In equation (27) μ is the viscosity of pore-fluid, whereas $\underline{\boldsymbol{g}}$ is the constant (i.e., uniform throughout the fluid domain) macroscopic gradient of pressure in some direction m, which means that

$$\underline{\boldsymbol{g}} = |\underline{\boldsymbol{g}}|\underline{\boldsymbol{e}}^{(m)}\,, \tag{30}$$

where $\underline{\boldsymbol{e}}^{(m)}$ is the unit vector along this direction.

It can be shown that the local velocity field is linearly related to the macroscopic pressure gradient, that is,

$$\underline{\boldsymbol{v}} = -\frac{\underline{\underline{\boldsymbol{k_0}}}}{\mu} \cdot \underline{\boldsymbol{g}}\,, \tag{31}$$

where $\underline{\underline{\boldsymbol{k_0}}}$ is the tensor field of (viscous) permeability. As a matter of fact, this relation is a local (microscopic) version of the well-known Darcy's law, which is yield after averaging.

Now, the following vector field is defined as the projection of the second-order tensor $\underline{\underline{\boldsymbol{k_0}}}$ onto the direction m:

$$\underline{\boldsymbol{k_0}}^{(m)} = \underline{\underline{\boldsymbol{k_0}}} \cdot \underline{\boldsymbol{e}}^{(m)}\,. \tag{32}$$

Using this definition and also the relation (30) for the "microscopic Darcy's law" (31) the following formula is obtained for the velocity vector

$$\underline{\boldsymbol{v}} = -\frac{|\underline{\boldsymbol{g}}|}{\mu}\,\underline{\boldsymbol{k_0}}^{(m)}\,, \tag{33}$$

which can be used for the equations of viscous incompressible flow (27), (28), and (29), so that eventually, the scaled Boundary-Value Problem is obtained as follows:

$$-\triangle\underline{\boldsymbol{k_0}}^{(m)} + \nabla q_{0(m)} = \underline{\boldsymbol{e}}^{(m)} \quad \text{in } \Omega_{\mathrm{f}}, \tag{34}$$

and

$$\nabla \cdot \underline{\boldsymbol{k_0}}^{(m)} = 0 \quad \text{in } \Omega_{\mathrm{f}}, \tag{35}$$

with boundary conditions to be satisfied on the solid walls

$$\underline{\boldsymbol{k_0}}^{(m)} = \underline{\boldsymbol{0}} \quad \text{on } \partial\Omega_{\mathrm{sf}}. \tag{36}$$

Here, the unknown fields are the vector field $\underline{\boldsymbol{k_0}}^{(m)}$ and the scalar field $q_{0(m)}$. Both are periodic over the fluid domain Ω_{f}. The vector field $\underline{\boldsymbol{k_0}}^{(m)}$ has dimension of permeability [m^2] and accordingly to the formula (33) it can be treated as the velocity field scaled by factor $-\mu/|\underline{\boldsymbol{g}}|$. Similarly, the scalar field $q_{0(m)}$ is defined as the scaled field of pressure

$$q_{0(m)} = -\frac{p}{|\underline{\boldsymbol{g}}|} \tag{37}$$

with dimension [m].

In order to determine the second-order tensor field of permeability $\underline{\underline{\boldsymbol{k_0}}}$ the scaled Boundary-Value Problem (34), (35), (36) must be solved three times for three mutually perpendicular directions $m = 1, 2, 3$, defining three orthogonal unit vectors $\underline{\boldsymbol{e}}^{(m)}$. Then, the components of this tensor field in the basis $\underline{\boldsymbol{e}}^{(m)} \otimes \underline{\boldsymbol{e}}^{(n)}$ $(m, n = 1, 2, 3)$ are defined as

$$k_{0(mn)} = k_{0(n)}^{(m)} , \tag{38}$$

where $k_{0(n)}^{(m)}$ are the components of vectors $\underline{\boldsymbol{k_0}}^{(m)}$ obtained as three independent solutions.

The macroscopic tensor of permeability is defined as the average of permeability field over the microscopic cell, and since this field is zero in the solid domain the final result is the average over the fluid domain scaled by the porosity factor:

$$\underline{\underline{\widehat{\boldsymbol{k_0}}}} = \phi \left\langle \underline{\underline{\boldsymbol{k_0}}} \right\rangle_{\mathrm{f}} . \tag{39}$$

This is the classical (static, viscous) permeability tensor used by the Darcy's law. It is static with respect to the dynamic generalization of permeability as a frequency-dependent function, and it may be explicitly called viscous to disambiguate from its thermal analogue.

In case of isotropy or when the wave propagation is simply considered in the direction m the scalar macroscopic permeability needs only to be calculated:

$$\widehat{k}_0 = \widehat{k}_{0(m)} = \phi \left\langle k_{0(m)}^{(m)} \right\rangle_{\mathrm{f}} . \tag{40}$$

This is in fact the limit of the dynamic viscous permeability function $\widehat{k}(\omega)$ for $\omega \to 0$.

Similarly to the classic parameter of tortuosity computed from the scaled analysis of electric conduction the static tortuosity (i.e., at 0 Hz) is given by

$$\alpha_0 = \alpha_{0(m)} = \frac{\left\langle \underline{\boldsymbol{k_0}}^{(m)} \cdot \underline{\boldsymbol{k_0}}^{(m)} \right\rangle_{\mathrm{f}}}{\left\langle \underline{\boldsymbol{k_0}}^{(m)} \right\rangle_{\mathrm{f}} \cdot \left\langle \underline{\boldsymbol{k_0}}^{(m)} \right\rangle_{\mathrm{f}}} . \tag{41}$$

E. Thermal conduction problem

The pressure fluctuations caused by acoustic waves induce some fluctuations of temperature inside the fluid., and therefore a heat flow. On the micro-scale the phenomenon is governed by the equation of harmonic thermal flow (for the complex amplitude of temperature T):

$$\kappa \triangle T - \mathrm{i}\omega C_{\mathrm{p}} \varrho_{\mathrm{f}} T = -\mathrm{i}\omega P \quad \text{in } \Omega_{\mathrm{f}}, \tag{42}$$

with isothermal boundary condition on solid walls

$$T = 0 \quad \text{on } \partial\Omega_{\mathrm{sf}}, \tag{43}$$

because the thermal conductivity of fluid in pores (typically, the air) is usually much lower than the one of solid. In equation (42) κ is the thermal conductivity of fluid in pores, whereas C_{p} is the specific heat at constant pressure; the heat transfer is caused by the harmonic change of macroscopic pressure with the amplitude P uniform in the whole fluid domain of cell.

It can be shown that when the solid frame is a thermostat the mean excess temperature in the air is proportional to the mean time derivative of the pressure, which in harmonic case equals $\mathrm{i}\omega P$. Thus, by the analogy to the "localised" Darcy's law (31) the following relation was proposed by Lafarge[14] which links the harmonic change of pressure inside pores of a porous medium with the temperature

$$T = \frac{k'}{\kappa} \mathrm{i}\omega P . \tag{44}$$

Here, k' is the thermal analogue of dynamic permeability. Unlike its viscous counterpart it is not a second-order tensor yet scalar field since the thermal flow equation described an omnidirectional dispersion of temperature. The dynamic "thermal permeability" filed $k'(\omega)$ shows how this temperature spread is allowed at particular frequency ω by the arrangement of solid walls.

Now, by using the relation (44) for the thermal flow problem (42) and (43), and also by taking into account that

$$\frac{C_{\mathrm{p}} \varrho_{\mathrm{f}}}{\kappa} = \frac{\mathrm{Pr}}{\nu} = \frac{1}{\nu'} , \tag{45}$$

the following scaled Boundary-Value Problem is obtained

$$-\triangle k' + \frac{\mathrm{i}\omega}{\nu'} k' = 1 \quad \text{in } \Omega_{\mathrm{f}}, \tag{46}$$

for the unknown field of dynamic "thermal permeability" k' which is periodic on Ω_{f} and must satisfy the homogeneous boundary condition on solid walls, i.e.:

$$k' = 0 \quad \text{on } \partial\Omega_{\mathrm{sf}}. \tag{47}$$

In that context the thermal dynamic permeability field k' is but a scaled field of temperature amplitude.

For the static case, or at very low frequencies when $\omega \to 0$, the Poisson equation is obtained from (46), that is:

$$-\triangle k_0' = 1 \quad \text{in } \Omega_{\mathrm{f}}, \tag{48}$$

with boundary condition

$$k_0' = 0 \quad \text{on } \partial\Omega_{\mathrm{sf}}. \tag{49}$$

Here, the unknown periodic field k_0' is the static "thermal permeability" and at the same time the limit of its dynamic counterpart at 0 Hz.

When the scaled problem of static thermal flow (48) with (49) is solved and the static field of "thermal permeability" k_0' is found, the macroscopic parameter of "thermal permeability" is calculated as the average of this field over the whole microscopic cell:

$$\widehat{k}_0' = \phi \langle k_0' \rangle_{\mathrm{f}} . \tag{50}$$

Finally, the static thermal tortuosity (i.e., the low frequency limit of the real part of dynamic thermal tortuosity) is computed as

$$\alpha_0' = \frac{\left\langle {k_0'}^2 \right\rangle_{\mathrm{f}}}{\langle k_0' \rangle_{\mathrm{f}}^{\,2}} . \tag{51}$$

V. FE ANALYSES FOR REGULAR SPHERE PACKING RVES WITH ADJUSTED POROSITY

The periodic RVEs based on the regular sphere packings SC, BCC, and FCC with the porosity adjusted to 42% – as described in Section III – served in finite-element analyses (briefly discussed below) to calculate the parameters of Johnson-Champoux-Allard-Pride-Lafarge model. The corresponding finite-element meshes

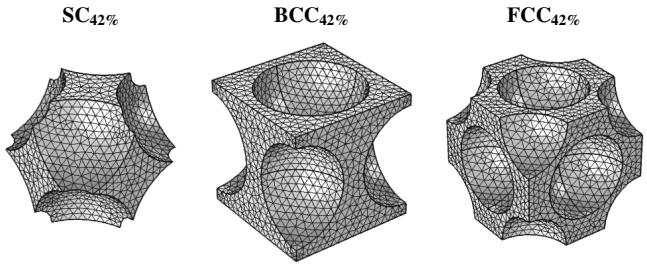

Figure 6: Finite element meshes of Representative Volume Elements (for media with porosity 42%)

generated over the fluid domains of the three representative cells are presented in Figure 6.

Figure 7 presents the viscous permeability field obtained for all three RVEs from the scaled Stokes flow driven by the uniform pressure gradient in the x-direction. These results were used to compute the corresponding parameter of viscous permeability $\widehat{k}_0$ as the volume average from the permeability field. It suffice only to make these calculations for one direction because each of the representative cells is identical with respect to three perpendicular directions which agrees very well with the assumption of macroscopic isotropy and causes the permeability tensor to be isotropic. From the same analysis also the parameter of viscous tortuosity at 0 Hz α_0 was determined. Both values are given in Table IV together with other parameters for the extended Johnson-Champoux-Allard-Pride-Lafarge model.

Table IV: Macroscopic parameters computed from the microstrucure RVEs with porosity 42%

Parameter Name – Symbol – Unit	Packing type – RVE SC42%	BCC42%	FCC42%
viscous permeability: $\widehat{k}_0$ [mm^2]	0.0546	0.0452	0.0393
thermal permeability: $\widehat{k}'_0$ [mm^2]	0.1459	0.0803	0.0834
tortuosity (at ∞ Hz): α_∞ [–]	1.5263	1.3245	1.3191
viscous tortuosity at 0 Hz: α_0 [–]	2.3052	1.9343	1.8371
thermal tortuosity at 0 Hz: α'_0 [–]	1.4438	1.3141	1.5238
viscous length: Λ [mm]	0.9900	1.1054	1.1197
thermal length: Λ' [mm]	1.5573	1.4268	1.4230

Apart from the porosity ϕ, among the other seven parameters shown in Table IV are the thermal analogue of permeability $\widehat{k}'_0$ and the thermal tortuosity at 0 Hz α'_0. Both are computed from the solution of the Poisson equation which results from scaling of the problem of stationary heat transfer in pore fluid with isothermal boundary conditions on the skeleton walls, driven by the unit heat source uniform in the whole fluid domain. The thermal permeability is calculated as the volume average from the thermal permeability fields (which are, as a matter of fact, the scaled fields of temperature) shown in Figure 8 as the results of finite element analyses.

The tortusity parameter α_∞ (i.e., the real part of the dynamic tortuosity limit as frequency goes to infinity) is computed from the solution of the Laplace problem as the average of the resulting potential field – shown in Figure 9 for three cases of periodic RVEs – caused by the (scaled electric) unit vector field uniform in the x-direction. As in the case of viscous permeability and Stokes problem, only one Laplace analysis was necessary here because of the directional identity of cells resulting in exact macroscopic isotropy. Form the same analysis the viscous characteristic length Λ is also calculated. The thermal characteristic length Λ' is determined directly from the geometry of RVE, as the doubled ratio of the fluid domain or pore volume to the total surface of pore walls.

It is easy to notice from Table IV that the corresponding parameters computed for the BCC and FCC representative cells are very similar to each other, and they visibly differ – though not very much – from the ones obtained in the SC case.

As described in Section B the parameters given in Table IV allow – by using the formulas of the Johnson-Champoux-Allard-Pride-Lafarge model – to determine the frequency-dependent effective density (which is the frequecny-dependent tortuosity characteristics multiplied by the density of air) and compressibility of the homogenised acoustic fluid macroscopically equivalent to the examined rigid porous medium filled with air. Firstly, however, some analytical estimates of these macroscopic parameters will be provided in the next Section.

VI. SELF-CONSISTENT ESTIMATES OF MACROSCOPIC PARAMETERS

In this Section the macroscopic parameters will be estimated using the so-called self-consistent method (SCM) based on a bicomposite spherical pattern[37,38]. In this method the local physics of the considered phenomenon is solved analytically in a generic pattern representative for the actual morphology, for the homogeneous macroscopic forcing term. The nature of the macroscopic behaviour is assumed and the energy equivalence between the generic pattern and the equivalent medium allows to estimate the macroscopic parameters.

The generic pattern used here is the bicomposite spherical pattern presented in Figure 10. It is in the shape of a sphere Ω with radius R containing an inner solid sphere with radius R_s surrounded by a spherical shell Ω_f filled with fluid. The solid sphere is rigid and the fluid is the pore-fluid (i.e., the air). The solid sphere radius will be assumed equal to the radius of the actual spherical beads used in the experimental test, that is, $R_\mathrm{s} = 5.9\,\mathrm{mm}/2 = 2.95\,\mathrm{mm}$. The radius of spherical cell must be related to the solid sphere radius in such a way so that the actual porosity $\phi = 0.42$ should be ensured, therefore, the ratio between the two radii should be defined as follows

$$\delta = \frac{R_\mathrm{s}}{R} = \sqrt[3]{\frac{\frac{4}{3}\pi R_\mathrm{s}^3}{\frac{4}{3}\pi R^3}} = \sqrt[3]{1-\phi}\,, \tag{52}$$

and in the considered case $\delta = 0.83396$, which means that $R = R_\mathrm{s}/\delta = 3.537\,\mathrm{mm}$. These values will be used for all the estimations computed below. They are, however, nearly identical (or very similar) with the generic values computed with respect to the Representative Volume Elements considered in this work using the approach in which the radius of the solid sphere in generic pattern is computed from the assumed porosity ϕ and the number of (identical) solid inclusions N_s in a cell of Representative Volume Element by assuming that its total volume V should be the same as the volume of the spherical cell in generic pattern; it means that the following relation is satisfied

$$\frac{4}{3}\pi R_\mathrm{s}^3 = \frac{(1-\phi)V}{N_\mathrm{s}}\,. \tag{53}$$

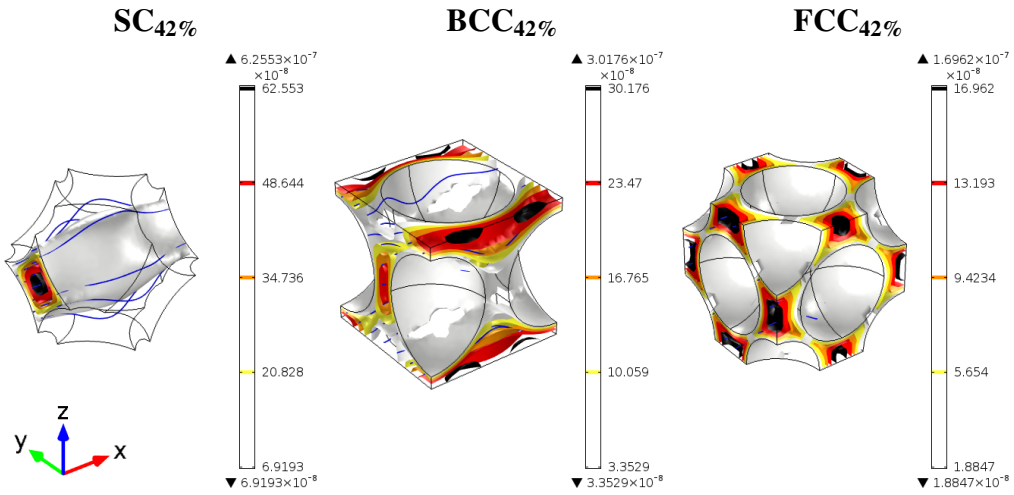

Figure 7: Results of FE analyses for various RVEs: the viscous permeability field $k_{0(11)}$ [m^2]

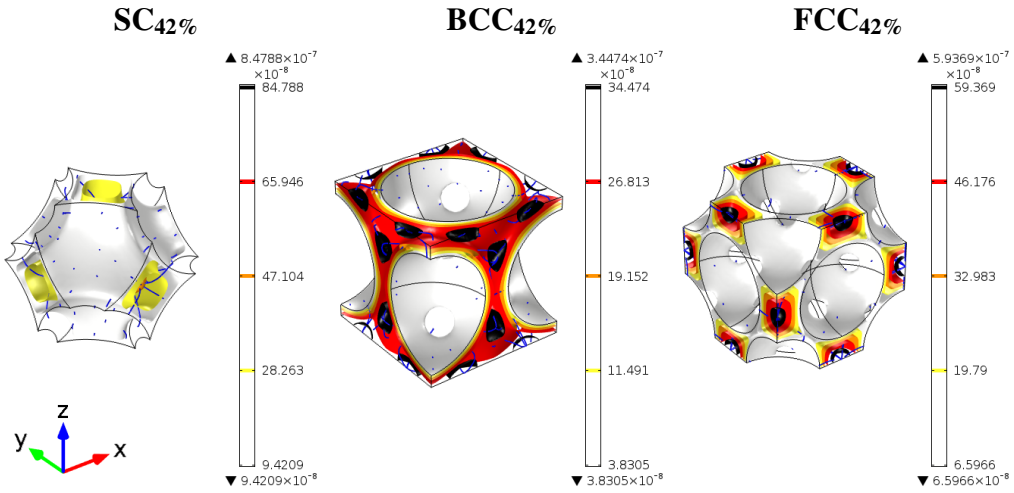

Figure 8: Results of FE analyses for various RVEs: the thermal permeability field k_0' [m^2]

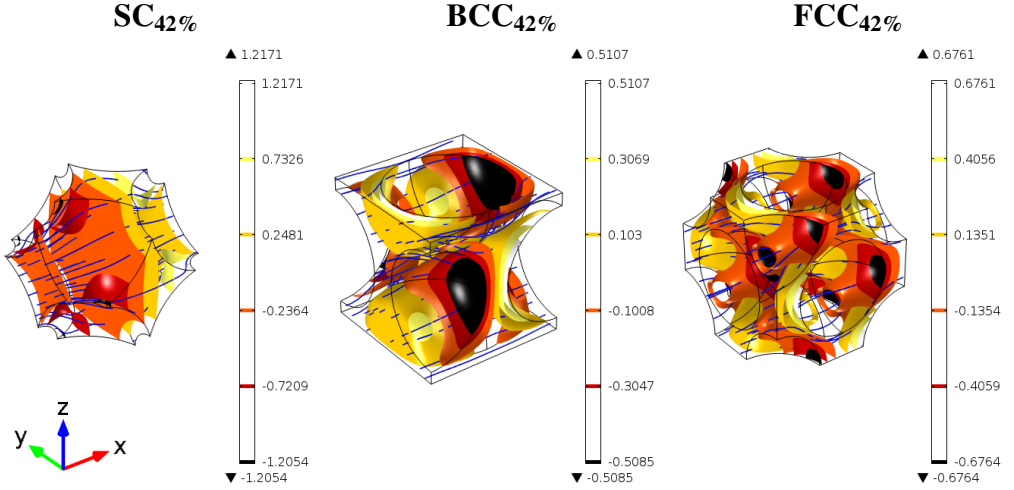

Figure 9: Results of FE analyses for various RVEs: the scaled potential field $q_{(1)}$ [mm]

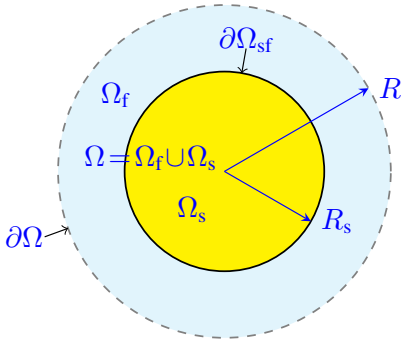

Figure 10: Bicomposite spherical pattern formed from a sphere Ω with radius R composed from an inner (rigid) solid sphere Ω_s with radius R_s surrounded by a spherical shell Ω_f filled with fluid

Table V: Generic features of spherical cells corresponding to the SC, BCC, and FCC sphere-packings with porosity adjusted to 42%

Generic parameter Name – Symbol – Unit	Packing type – RVE $SC_{42\%}$	$BCC_{42\%}$	$FCC_{42\%}$
volume of cell or RVE: V [mm^3]	181.71	371.11	741.37
number of solids in RVE: N_s [–]	1	2	4
solid-to-cell radius ratio: δ [–]	$\longrightarrow$	0.83396	$\longleftarrow$
solid sphere radius: R_s [mm]	2.9302	2.9508	2.9497
spherical cell radius: R [mm]	3.5137	3.5383	3.5369

In reference to the three RVEs considered in the previous Sections (using the data from Table III), the generic features of the corresponding bicomposite spherical cells are computed and listed in Table V. One should notice that the solid sphere and the whole cell radii are (nearly) identical with the values determined above, especially, for the cells corresponding to the $BCC_{42\%}$ or $FCC_{42\%}$ RVEs (some small discrepancies in case of the radii corresponding to the $SC_{42\%}$ RVE result mainly from the fact that in this periodic micro-morphology the rigid spheres are slightly overlapping).

The three generic parameters: the porosity ϕ, the ratio of solid sphere radius to the spherical cell radius δ, and the spherical bicomposite cell radius R, will be used in the formulas for self-consistent estimates of macroscopic parameters.

The consistent estimate of the (dynamic) viscous permeability is based on the analytical solution of the incompressible viscous flow through the spherical cell with the no-slip boundary conditions on the solid sphere surface $\partial\Omega_{sf}$; and the flow is driven by the uniform pressure gradient. It is the same problem as in the case of finite element analyses on periodic RVEs, however, the simplistic generic pattern of local geometry is used instead and the periodic conditions are replaced by the energy consistency constraints on the spherical cell boundary $\partial\Omega$. Eventually, this viscous and kinetic energy consistency between the microscopic and macroscopic description leads to the following alternative: (1) either the shear stress vanishes uniformly and the stress vector at the boundary $\partial\Omega$ matches the macroscopic (Darcy) pressure, or (2) the tangential, and thus also the total micro- and macroscopic velocities are equal on the cell boundary $\partial\Omega$. The first assumption leads to the so-called P-estimate, whereas the second one leads to the V-estimate. Finally, the so-called C-estimate results from the "cell" model assumption of vanishing vorticity at the boundary $\partial\Omega$, which means that the fluid pressure (not the stress) at the boundary equals to the macroscopic one (i.e., the Darcy pressure). These estimates are found for the general dynamic (harmonic) case of the viscous flow, and in the quasi-static regime (i.e., at low frequency, when the viscous effects dominate the inertial ones) they lead to the following P-, C- and V-estimation formulas[37,38] for the intrinsic (static viscous) permeability:

$$\frac{\widehat{k}_{0(\mathrm{eP})}}{R^2} = \frac{2 - 3\delta + 3\delta^5 - 2\delta^6}{9\delta + 6\delta^6}\,, \tag{54}$$

$$\frac{\widehat{k}_{0(\mathrm{eC})}}{R^2} = \frac{10 - 18\delta + 10\delta^3 - 2\delta^6}{45\delta}\,, \tag{55}$$

$$\frac{\widehat{k}_{0(\mathrm{eV})}}{R^2} = \frac{4 - 9\delta + 10\delta^3 - 9\delta^5 + 4\delta^6}{18\delta - 18\delta^6}\,. \tag{56}$$

In case of the tortuosity parameter the P-, C- and V-estimates are derived from the limit case of high-frequency behaviour, when the inertial effects dominate and the viscous ones are confined to a viscous layer, and thus, they lead to the same value which depends only on porosity (since the tortuosity may be derived from a perfect flow, where the interface conditions involve only the normal/radial component of velocity idependent on the P-, V- or C-assumption)[37,38]:

$$\alpha_{\infty(\mathrm{e})} = 1 + \frac{\delta^3}{2} = \frac{3 - \phi}{2}\,. \tag{57}$$

Finally, the P- or C-estimate of the viscous characteristic length is[37]

$$\frac{\Lambda_{(\mathrm{eP\ or\ C})}}{R} = \frac{4\phi}{9(1-\phi)}\alpha_{\infty(\mathrm{e})} = \frac{2\phi(3-\phi)}{9(1-\phi)}\,, \tag{58}$$

while the V-estimate reads[37]

$$\frac{\Lambda_{(\mathrm{eV})}}{R} = \frac{1}{1+\delta^4}\frac{\Lambda_{(\mathrm{eP})}}{R}\,. \tag{59}$$

The (dynamic) thermal permeability is estimated from the analytical solution of the same problem (46) as in the case of general periodic micro-geometry, however, set up in the fluid shell Ω_f of the generic spherical bicomposite cell Ω, with homogeneous ("isothermal") boundary conditions on the solid sphere surface $\partial\Omega_{sf}$. Again, the main difference (apart from the simple geometry pattern) is the consistency condition on the boundary $\partial\Omega$, which replaces the periodic condition. Eventually, in the quasi-static regime (i.e., at low frequencies, when the thermal conduction dominates the inertial effects) the following estimation of (static) thermal permeability is achieved[38]

$$\frac{\widehat{k}'_{0(\mathrm{e})}}{R} = \frac{3}{2\phi}\frac{\widehat{k}_{0(\mathrm{eC})}}{R}\,, \tag{60}$$

which is presented here in relation to the C-estimate of viscous permeability $\widehat{k}_{0(\mathrm{eC})}$, because of the similarity in analytical solutions. The thermal characteristic length is estimated as[38]

$$\frac{\Lambda'_{(\mathrm{e})}}{R} = \frac{2\phi}{3(1-\phi)}\,. \tag{61}$$

Table VI lists the estimates of macroscopic parameters computed (for the radius of spherical cell $R = 3.537$ mm) from the formulas presented above. In case of "viscous" parameters the three estimates, P-, C-, and V- are provided. The estimated values $\alpha_{0(\mathrm{e})}$ for the viscous tortuosity at 0 Hz are taken from Figure 6 in work by Boutin and Geindreau[38]. (The estimates for the thermal tortuosity at 0 Hz will be assumed from the relevant $FCC_{42\%}$ finite element analysis.) Some relevant finite element calculations from Table IV are also recalled. A comparison reveals a good conformity

Table VI: Estimates of macroscopic parameters from the generic spherical cell with porosity 42% and some corresponding FE results from Table IV

Estimated parameter Name – Symbol – Unit	Estimate type P	C	V	FE calculations (S: $SC_{42\%}$, F: $FCC_{42\%}$)
viscous permeability: $\widehat{k}_{0(e)}$ [mm^2]	0.0466	0.0387	0.0134	0.0546 (S), 0.0393 (F)
thermal permeability: $\widehat{k}'_{0(e)}$ [mm^2]	⟶	0.1363	⟵	0.1459 (S)
tortuosity (at ∞ Hz): $\alpha_{\infty(e)}$ [–]	⟶	1.29	⟵	1.319 (F)
viscous tortuosity at 0 Hz: $\alpha_{0(e)}$ [–]	1.70	1.65	1.45	1.837 (F)
viscous length: $\Lambda_{(e)}$ [mm]	⟶	1.2246	0.8254	1.120 (F), 0.990 (S)
thermal length: $\Lambda'_{(e)}$ [mm]	⟶	1.4240	⟵	1.423 (F)

of the C-estimate of intrinsic permeability, as well as the estimates of other parameters – with the corresponding $FCC_{42\%}$ results; this is with an exception of the thermal permeability estimate which tends to be close to the finite element result computed from the $SC_{42\%}$ RVE (also the V-estimate of viscous length is closer to the $SC_{42\%}$ result, although the P- or C-estimates are again very close to the $FCC_{42\%}$ result). These observations will be of importance below when the acoustic absorption estimates will be confronted with the measurement results.

VII. MICROSTRUCTURE-BASED MODELLING OF SOUND ABSORPTION IN LAYERS OF RIGID SPHERICAL BEADS VALIDATED BY THE EXPERIMENTAL TESTS

From the characteristic functions of effective density and compressibility computed using the Johnson-Champoux-Allard-Pride-Lafarge approximations[10,11] based on parameters from Table IV (computed from the microstructural finite element analyses) or their estimations from Table VI (calculated analytically), the frequency-dependent complex function of effective speed of sound $c_e(\omega)$ in the dispersive fluid equivalent to porous medium can be calculated using formula (4). The real and imaginary parts of this effective characteristics, divided by the speed of sound in air c_f (i.e., the actual fluid in pores), are presented in Figure 11 for all three numerical cases based on periodic RVEs as well as the three analytical estimates. First, it should be observed that the $BCC_{42\%}$ and $FCC_{42\%}$ results almost overlap, whereas the $SC_{42\%}$ result differs from them by a few percent. The P- and C-estimates are nearly identical and the V-estimate differs from them slightly in the real part, and more substantially in the imaginary part. Moreover, when considering the real part of the speed-of-sound ratio, all the three estimates are placed between the numerical result of the $SC_{42\%}$ RVE and the results obtained from the $BCC_{42\%}$ or $FCC_{42\%}$ RVE. On the other hand, in case of the imaginary part, it is the numerical results which are found between the limiting cases of the V-estimate and the P- or C- estimates. This observations are in some conformity with the fact observed above that the estimate of thermal permeability is not far from the $SC_{42\%}$ calculation, whereas the estimations of other parameters are rather similar with the $FCC_{42\%}$ results.

This speed of sound characteristics is used in the Helmholtz equation of time-harmonic acoustics solved for the configuration of a porous layer modelled as equivalent fluid fixed on a rigid wall with a plane harmonic acoustic wave excitation acting on the free surface. In that way, the acoustic pressure and velocity fields are found analytically in the layer for the relevant frequency range from 100 Hz to 6.4 kHz. Knowing the acoustic pressure and velocity, in particular, at the surface of the layer, the surface acoustic impedance can be calculated, and then the complex reflection coefficient and the real-valued acoustic absorption coefficient (see, for example Zielinski[51,52]).

The numerical procedure described above was applied for three porous layers with the same porosity of 42% and different height (thickness), namely: 41 mm, 106 mm, and finally 200 mm. These were actually the exact heights of layers measured in the vertically-positioned impedance tubes (see Figure 2). Therefore, the numerical calculations based on the multiscale modelling involving microstructure finite element analyses could be compared with the corresponding experimental results. For the purpose of this comparison, in case of each layer the results of microstructure calculations for three types of Representative Volume Elements were used, namely, for the RVEs based on SC, BCC, and FCC sphere packings with adjusted porosity of 42%. Finally, the results based on self-consistent estimates derived from the spherical bicomposite cell (with porosity 42%) are also provided.

Figure 12 shows the sound absorption of porous layer with thickness (height) of 41 mm. The acoustic absorption is especially good in some frequency ranges around 1700 Hz and 5200 Hz. These characteristic features of the experimental absorption curve are very well represented also by modelling results. As a matter of fact, the absorption curves obtained from numerical modelling are in very good agreement with the experimental result, although in general, the numerically computed absorption is slightly inferior than the one found experimentally. Moreover, one should observe that the two best-performance peaks in the numerical curve computed from the $SC_{42\%}$ RVE are slightly shifted to the left in the frequency domain, whereas the peaks computed from the $BCC_{42\%}$ or $FCC_{42\%}$ RVEs are slightly shifted to the right. However, it should be recalled now that in the first numerical case, that is for the $SC_{42\%}$ RVE, the spheres were slightly overlapping, whereas in the remaining two cases, that is for the $BCC_{42\%}$ or $FCC_{42\%}$ RVEs, the spheres were shifted apart leaving always some narrow space between them. In reality some of the spherical beads are in contact which may be seen as an intermediate case between the overlapping case and the cases without contact – and thus, the correct representative experimental results tend to be in the middle of the two limiting numerical cases. This reasoning seems to be somehow confirmed by the curves obtained from the self-consistent estimates. The V-estimate seems to be the closest to the experimental result, although the P- and C-estimates are rather inferior than the numerical findings. However, all three estimates have peaks in absorption at very similar frequencies as the measurements, that is, in-between the $SC_{42\%}$ and $FCC_{42\%}$ (or $BCC_{42\%}$) cases. Since the estimated thermal permeability was rather close to the $SC_{42\%}$ result, whereas the other estimated parameters were similar with the

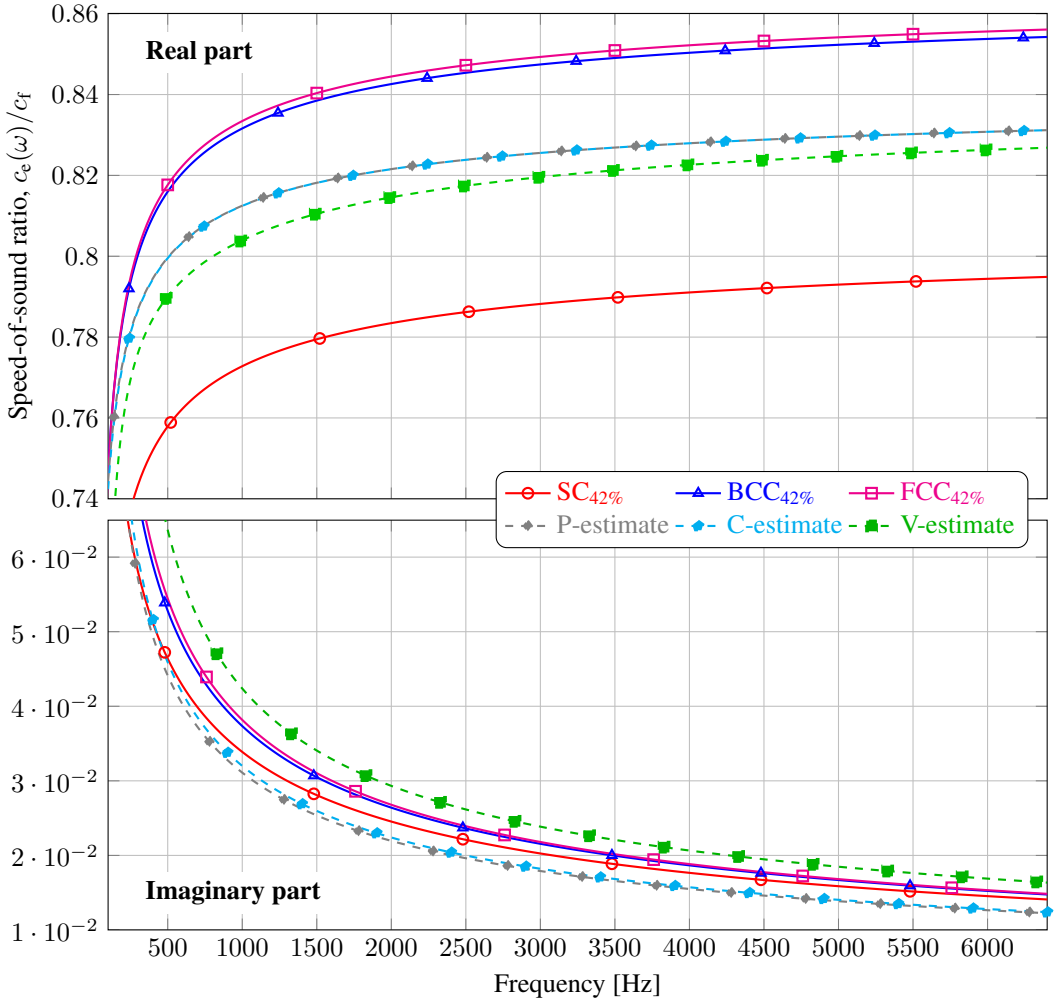

Figure 11: The ratio of the effective speed of sound to the speed of sound of pore-fluid

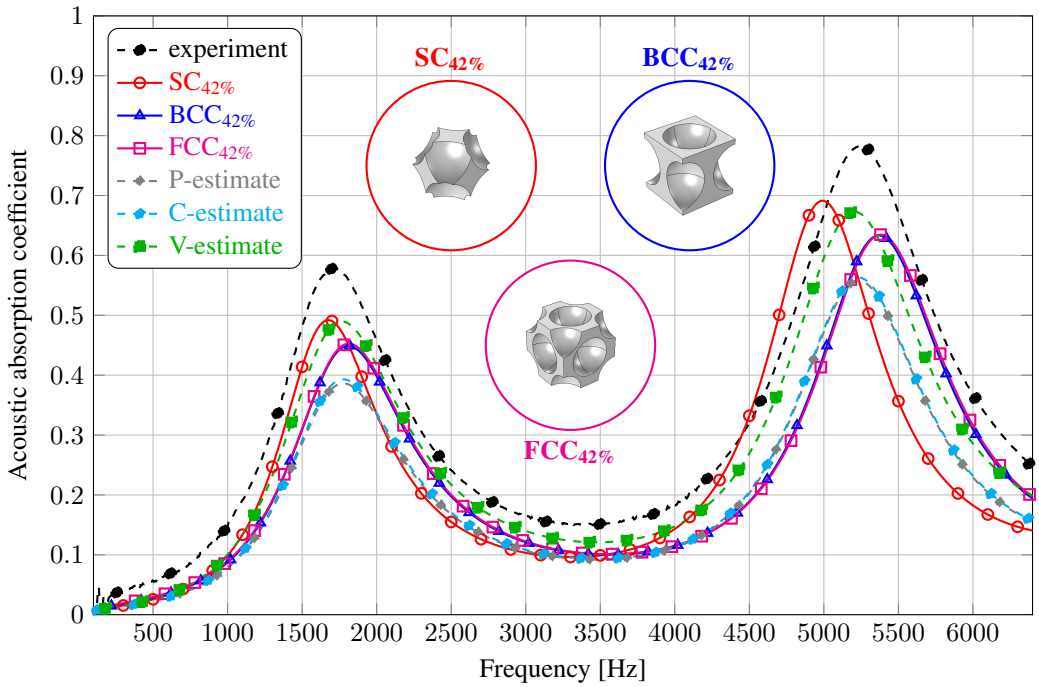

Figure 12: Acoustic absorption of 41 mm-thick layer of rigid spheres (beads): the multiscale modelling results vs. experiment

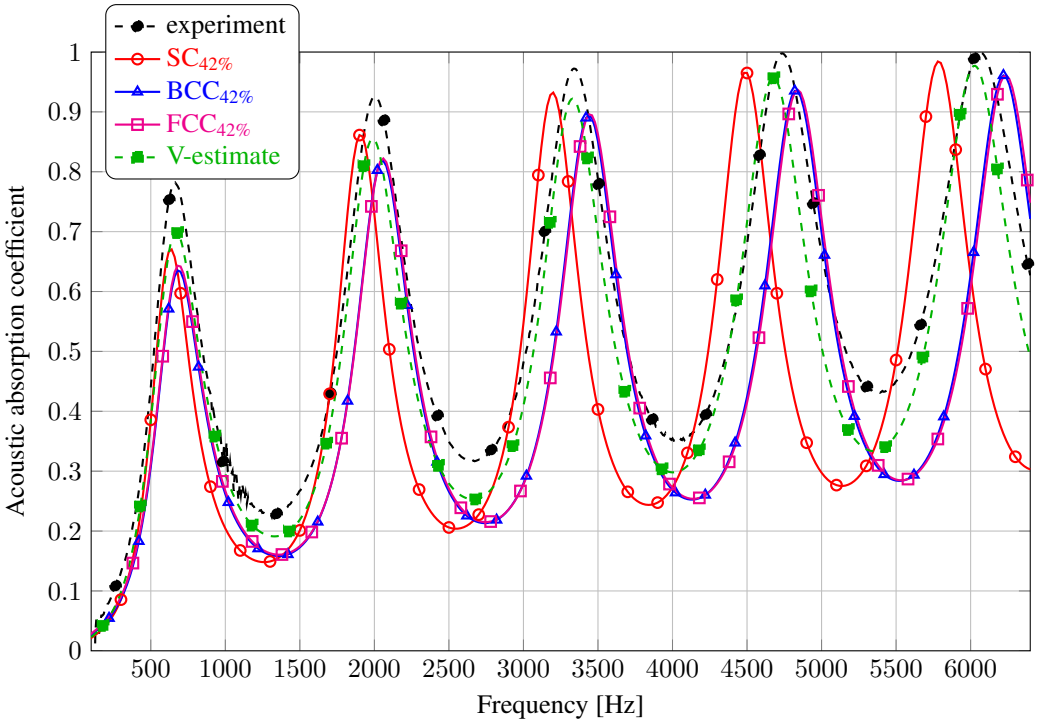

Figure 13: Acoustic absorption of 106 mm-thick layer of rigid spheres (beads): the multiscale modelling results vs. experiment

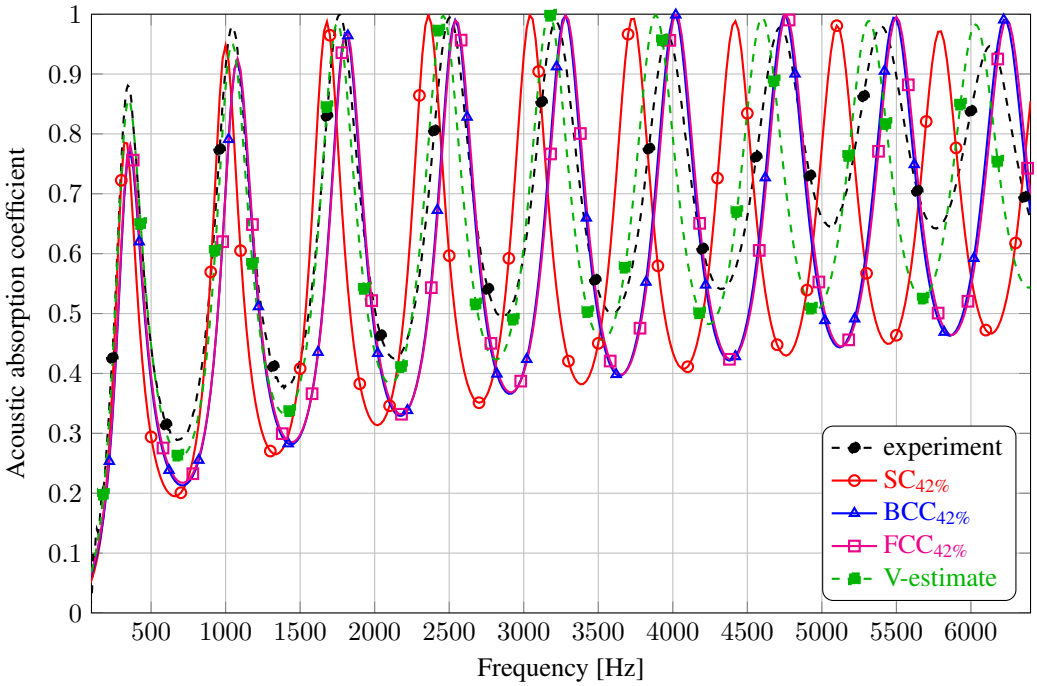

Figure 14: Acoustic absorption of 200 mm-thick layer of rigid spheres (beads): the multiscale modelling results vs. experiment

$FCC_{42\%}$ calculations, it seems that the $SC_{42\%}$ RVE tends to be more correct with respect to thermal transport, whereas the $FCC_{42\%}$ or $BCC_{42\%}$ RVEs allow for correct estimations of intrinsic permeability and tortuosity, that is, the properties of fluid flow through porous medium. In the actual layers, because of the tube constraints and rather loose packing some larger spaces may be formed between some of the beads which allows for higher thermal permeability than the one previewed by the regular FCC or BCC packings. On the other hand, as points out the V-estimate the actual viscous permeability seems to be even inferior than the lowest numerical finding based on the $FCC_{42\%}$ RVE, whereas the viscous characteristic length is somehow between the FCC/$BCC_{42\%}$ results (with spheres shifted apart) and the $SC_{42\%}$ one (with overlapping spheres).

Similar observations can be made in case of the sound absorption of thicker layers. Figure 13 presents the results obtained for the layer of spherical beads with thickness (height) of 106 mm: in the frequency range from 100 Hz to 6.4 kHz there are 5 performance peaks starting at about 0.7 kHz and then successively re-

appearing after additional approximately 1.35 kHz. The peaks of the experimental curve are repeated by the curves calculated numerically, however, in case of the solution found from the $SC_{42\%}$ RVE, when the frequency increases, the peaks at those higher frequencies tend to be more and more significantly shifted to the left in the frequency domain. On the other hand, the peaks in curves found on the basis of the $BCC_{42\%}$ or $FCC_{42\%}$ RVEs tend to be only very slightly shifted to the right. The same conclusions can be drawn when comparing the results measured and computed for the 200 mm-thick layer presented in Figure 14. There are now 9 best performance peaks of the acoustic absorption in the considered frequency range, rather well represented by the numerical curves computed from the simulations based on the $BCC_{42\%}$ or $FCC_{42\%}$ RVEs. Lower frequency peaks in the acoustic absorption curve obtained from the $SC_{42\%}$ simulations are also in a good agreement with the experimental results, while the higher frequency peaks are significantly shifted to a lower range. For the sake of legibility, only V-estimate is presented in Figures 13 and 14, since it is very close to the corresponding measurements, and the other estimates (i.e., the P- or C-estimate) were in general worse than the numerical results obtained from the $FCC_{42\%}$ or $BCC_{42\%}$ RVEs.

It is easy to notice that the discrepancies between numerical simulations and experimental results are bigger for thicker layers. A rational explanation is that the sound waves need to pass a longer distance through a thicker porous material so that the errors coming from the idealised numerical representations of more random porous microstructure are summed up, and the effect is even doubled by the fact that it considers both the incident and reflected waves. More obvious is the fact that the discrepancies appear rather in a higher frequency range where the wavelengths are shorter and the effects contributing to the acoustic wave absorption are more influenced by variations in the characteristic dimensions of the microstructure of porous medium which is rather simplified by the regular representations used in the modelling.

VIII. CONCLUSIONS

Representative Volume Elements based on regular sphere packings of the SC, BCC, and FCC types were used for the hybrid multiscale modelling of acoustic absorption in porous layers composed of quasi-randomly packed rigid plastic spherical beads with diameter 5.9 mm. The porosity of RVEs was adjusted to the exact value of 42% (found experimentally) by shifting the spheres apart – in case of the BCC or FCC packings – or by allowing for small overlapping – in case of the SC packing. This approach proved to be sufficient for the multiscale modelling of the problem using comparatively simple RVEs, suitable for very efficient finite element calculations. It was also confronted with the self-consistent estimates based on the spherical bicomposite cell.

As a matter of fact, the results obtained for the $BCC_{42\%}$ and $FCC_{42\%}$ packings are almost the same and they tend to be in a good accordance with the experimental results. They are better than the results based on the P- or C-estimate, however, the V-estimate seems to be the closest with the experimental findings. The results computed using the RVE based on the $SC_{42\%}$ packing are still good for thinner layers; however, in case of thicker layers the acoustic absorption is estimated more or less correctly only in a lower part of the considered frequency range. The cause for the discrepancies at higher frequencies is a poorer scale separation and a vulnerability of shorter waves for the variations in characteristic dimensions of microstructure, not correctly represented by the idealised regular RVE. It is crucial especially for thicker layers where the passing distance of waves is longer so that the discrepancies can accumulate. Moreover, one should remember that the $SC_{42\%}$ packing allows for overlapping of the spheres which is nowhere present in the actual microstructure of porous medium composed of spherical plastic beads poured randomly into the measurement tubes.

Nevertheless, both, the numerical calculations and the analytical estimates give a systematic underestimation of sound absorption when compared to the measurements. This difference tends to be more pronounced at higher frequencies where the wavelength of sound waves in porous medium is getting shorter. The plausible explanation of this fact may be a poor realisation of the scale separation assumption (a fundamental assumption taken by the model). As a matter of fact, the spherical beads are 5.9 mm in diameter and some of the actual air spaces in the measured layers of beads loosely packed in a tube may be fairly large in size (a few milimeters) and larger than the distances in regular sphere packings or bicomposite cell. The wavelengths (which are, for example, 97 mm at 3 kHz and 58 mm at 5 kHz) are still larger than the characteristic dimensions of pores yet the order of scale separation is rather poor. This should result in some additional dissipative mechanisms not present in the model, which at even higher frequencies would lead to scattering or trapping phenomena of very short waves.

ACKNOWLEDGMENTS

Financial support of Structural Funds in the Operational Programme – Innovative Economy (IE OP), financed from the European Regional Development Fund – Project "Modern Material Technologies in Aerospace Industry", No. POIG.01.01.02-00-015/08, is gratefully acknowledged. This work was carried out in part using computing resources of the "*GRAFEN*" supercomputing cluster at IPPT PAN, from the computer infrastructure of *Biocentrum Ochota*.

[1] M. E. Delany and E. N. Bazley, "Acoustical properties of fibrous absorbent materials," Appl. Acoust. **3**, 105–116 (1970).

[2] Y. Miki, "Acoustical properties of porous materials – Generalizations of empirical models," J. Acoust. Soc. Jpn. **11**, 19–24 (1990).

[3] Y. Miki, "Acoustical properties of porous materials – Modifications of Delany-Bazley models," J. Acoust. Soc. Jpn. **11**, 25–28 (1990).

[4] N. Voronina, "An empirical model for rigid frame porous materials with high porosity," Appl. Acoust. **51**, 181–198 (1997).

[5] N. Voronina, "An empirical model for rigid-frame porous materials with low porosity," Appl. Acoust. **58**, 295–304 (1999).

[6] D. L. Johnson, J. Koplik, and R. Dashen, "Theory of dynamic permeability and tortuosity in fluid-saturated porous media," J. Fluid Mech. **176**, 379–402 (1987).

[7] Y. Champoux and J.-F. Allard, "Dynamic tortuosity and bulk modulus in air-saturated porous media," J. Appl. Phys. **70**, 1975–1979 (1991).

[8] S. Kostek, L. M. Schwartz, and D. L. Johnson, "Fluid permeability in porous media: Comparison of electrical with hydrodynamical calculations," Phys. Rev. B **45**, 186–195 (1992).

[9] J.-F. Allard and Y. Champoux, "New empirical equations for sound propagation in rigid frame fibrous materials," J. Acoust. Soc. Am. **91**, 3346–3353 (1992).

[10] J. F. Allard and N. Atalla, *Propagation of Sound in Porous Media: Modelling Sound Absorbing Materials, Second Edition* (Wiley, 2009).

[11] APMR – Acoustical Porous Material Recipes. http://apmr.matelys.com/

[12] S. R. Pride, A. F. Gangi, and F. D. Morgan, "Deriving the equations of motion for porous isotropic media," J. Acoust. Soc. Am. **92**, 3278–3290 (1992).

[13] S. R. Pride, F. D. Morgan, and A. F. Gangi, "Drag forces of porous-medium acoustics," Physical Review B **47**, 1964–4978 (1993).

[14] D. Lafarge, P. Lemarinier, J. F. Allard, and V. Tarnow, "Dynamic compressibility of air in porous structures at audible frequencies," J. Acoust. Soc. Am. **102**, 1995–2006 (1997).

[15] M. Cieszko, R. Drelich, and M. Pakula, "Acoustic wave propagation in equivalent fluid macroscopically inhomogeneous materials," J. Acoust. Soc. Am. **132**, 2970–2977 (2012).

[16] K. Attenborough, "Acoustical characteristics of rigid fibrous absorbents and granular materials," J. Acoust. Soc. Am. **73**, 785–799 (1983).

[17] K. Attenborough, "On the acoustic slow wave in air-filled granular media," J. Acoust. Soc. Am. **81**, 93–102 (1987).

[18] N. N. Voronina and K. V. Horoshenkov, "A new empirical model for the acoustic properties of loose granular media," Appl. Acoust. **64**, 415–435 (2003).

[19] K. V. Horoshenkov and M. J. Swift, "The acoustic properties of granular materials with pore size distribution close to log-normal," J. Acoust. Soc. Am. **110**, 2371–2378 (2001).

[20] K. V. Horoshenkov, K. Attenborough, and S. N. Chandler-Wilde, "Padé approximant for the acoustical properties of rigid frame porous media with pore size distribution.pdf," J. Acoust. Soc. Am. **104**, 1198–1209 (1998).

[21] E. Charlaix, A. P. Kushnick, and J. P. Stokes, "Experimental study of dynamic permeability in porous media," Phys. Rev. Lett. **61**, 1595–1598 (1988).

[22] A. M. Chapman and J. J. L. Higdon, "Oscillatory stokes flow in periodic porous media," Phys. Fluids A **4**, 2099–2166 (1992).

[23] J. F. Allard, M. Henry, J. Tizianel, L. Kelders, and W. Lauriks, "Sound propagation in air-saturated random packings of beads," J. Acoust. Soc. Am. **104**, 2004–2007 (1998).

[24] J. G. Berryman, "Random close packing of hard spheres and disks," Phys. Rev. A: At., Mol., Opt. Phys. **27**, 1053–1061 (1983).

[25] S. Torquato, T. Truskett, and P. G. Debenedetti, "Is random close packing of spheres well defined?" Phys. Rev. Lett. **84**, 2064–2067 (2000).

[26] V. Tarnow, "Calculation of the dynamic air flow resistivity of fiber materials," J. Acoust. Soc. Am. **102**, 1680–1688 (1997).

[27] O. Umnova, K. Attenborough, and K. M. Li, "Cell model calculations of dynamic drag parameters in packings of spheres," J. Acoust. Soc. Am. **107**, 3113–3119 (2000).

[28] S. Gasser, F. Paun, and Y. Bréchet, "Absorptive properties of rigid porous media: Application to face centered cubic sphere packing," J. Acoust. Soc. Am. **117**, 2090–2099 (2005).

[29] C. Perrot, R. Panneton, and X. Olny, "Periodic unit cell reconstruction of porous media: Application to open-cell aluminum foams," J. Appl. Phys. **101**, 113538 (2007).

[30] C. Perrot, F. Chevillotte, and R. Panneton, "Dynamic viscous permeability of an open-cell aluminum foam: Computations versus experiments," J. Appl. Phys. **103**, 024909 (2008).

[31] C. Perrot, F. Chevillotte, M. T. Hoang, G. Bonnet, F.-X. Bécot, L. Gautron, and A. Duval, "Microstructure, transport, and acoustic properties of open-cell foam samples. experiments and three-dimensional numerical simulations," J. Appl. Phys. **111**, 014911 (2012).

[32] C. Perrot, F. Chevillotte, and R. Panneton, "Bottom-up approach for microstructure optimization of sound absorbing materials," J. Acoust. Soc. Am. **124**, 940–948 (2008).

[33] A. Cortis, D. M. J. Smeulders, J. L. Guermond, and D. Lafarge, "Influence of pore roughness on high-frequency permeability," Phys. Fluids **15**, 1766–1775 (2003).

[34] F. Chevillotte, C. Perrot, and R. Panneton, "Microstructure based model for sound absorption predictions of perforated closed-cell metallic foams," J. Acoust. Soc. Am. **128**, 1766–1776 (2010).

[35] F. Chevillotte, C. Perrot, and E. Guillon, "A direct link between microstructure and acoustical macro-behavior of real double porosity foams," J. Acoust. Soc. Am. **134**, 4681–4690 (2013).

[36] M. T. Hoang and C. Perrot, "Solid films and transports in cellular foams," J. Appl. Phys. **112**, 054911 (2012).

[37] C. Boutin and C. Geindreau, "Estimates and bounds of dynamic permeability of granular media," J. Acoust. Soc. Am. **124**, 3576–3593 (2008).

[38] C. Boutin and C. Geindreau, "Periodic homogenization and consistent estimates of transport parameters through sphere and polyhedron packings in the whole porosity range," Phys. Rev. E: Stat., Nonlinear, Soft Matter Phys. **82**, 036313 (2010).

[39] C.-Y. Lee, M. J. Leamy, and J. H. Nadler, "Acoustic absorption calculation in irreducible porous media: A unified computational approach," J. Acoust. Soc. Am. **126**, 1862–1870 (2009).

[40] "ISO 10534-2: Determination of sound absorption coefficient and impedance in impedance tubes," (1998).

[41] J.-P. Dalmont, "Acoustic impedance measurement, Part I: A review. Part II: A new calibration method," J. Sound Vib. **243**, 427–459 (2001).

[42] E. Sanchez-Palencia, *Non-Homogenous Media and Vibration Theory*, Lecture Notes in Physics, Vol. 127 (Springer, 1980).

[43] J. Auriault, "Dynamic behaviour of a porous medium saturated by a Newtonain fluid," Int. J. Engng. Sci. **18**, 775–785 (1980).

[44] J.-L. Auriault, L. Borne, and R. Chambon, "Dynamics of porous saturated media, checking of the generalized law of Darcy," J. Acoust. Soc. Am. **77**, 1641–1650 (1985).

[45] A. Cortis and J. G. Berryman, "Frequency-dependent viscous flow in channels with fractal rough surfaces," Phys. Fluids **22**, 053603 (2010).

[46] M. Cieszko, "Influence of a rigid skeleton pore structure on wave-propagation in a fluid-filling porous-medium," Transport Porous Med. **9**, 61–71 (1992).

[47] D. Lafarge, "Materials and acoustics handbook," (ISTE, Wiley, 2009) Chap. 6: The equivalent fluid model, pp. 167–201.

[48] R. J. S. Brown, "Connection between formation factor for electrical resistivity and fluid-solid coupling factor in biot's equations for acoustic waves in fluid-filled porous media," Geophysics **45**, 1269–1275 (1980).

[49] M. Avellaneda and S. Torquato, "Rigorous link between fluid permeability, electrical conductivity, and relaxation times for transport in porous media," Phys. Fluids A **3**, 2529–2540 (1991).

[50] D. Lafarge, "Comments on "rigorous link between fluid permeability, electric conductivity, and relaxation times for transport in porous media"," Phys. Fluids **5**, 500–502 (1993).

[51] T. G. Zieliński, "Numerical investigation of active porous composites with enhanced acoustic absorption," J. Sound Vib. **330**, 5292–5308 (2011).

[52] T. G. Zieliński, "Inverse identification and microscopic estimation of parameters for models of sound absorption in porous ceramics," in *Proceedings of International Conference on Noise and Vibration Engineering (ISMA2012) / International Conference on Uncertainty in Structural Dynamics (USD2012)*, edited by P. Sas, D. Moens, and S. Jonckheere (2012) pp. 95–108.